An adaptive sparse deconvolution method for distinguishing the overlapping echoes of ultrasonic guided waves for pipeline crack inspection

OPEN ACCESS
IOP Publishing
Measurement Science and Technology
Meas. Sci. Technol. **28** (2017) 035002 (14pp)
doi:10.1088/1361-6501/aa52ae

An adaptive sparse deconvolution method for distinguishing the overlapping echoes of ultrasonic guided waves for pipeline crack inspection

Yong Chang[1,2], Yanyang Zi[1,2], Jiyuan Zhao[1,3], Zhe Yang[1,2], Wangpeng He[4] and Hailiang Sun[5]

[1] School of Mechanical Engineering, Xi'an Jiaotong University, Xi'an, People's Republic of China
[2] The State Key Laboratory for Manufacturing System Engineering, Xi'an Jiaotong University, Xi'an, People's Republic of China
[3] Collaborative Innovation Center of High-end Manufacturing Equipment, Xi'an Jiaotong University, Xi'an, People's Republic of China
[4] School of Aerospace Science and Technology, Xidian University, Xi'an 710071, People's Republic of China
[5] Beijing Institute of Astronautical Systems Engineering, Beijing, 100076, People's Republic of China

E-mail: ziyy@mail.xjtu.edu.cn

Received 29 July 2016, revised 22 November 2016
Accepted for publication 8 December 2016
Published 13 January 2017

Abstract

In guided wave pipeline inspection, echoes reflected from closely spaced reflectors generally overlap, meaning useful information is lost. To solve the overlapping problem, sparse deconvolution methods have been developed in the past decade. However, conventional sparse deconvolution methods have limitations in handling guided wave signals, because the input signal is directly used as the prototype of the convolution matrix, without considering the waveform change caused by the dispersion properties of the guided wave. In this paper, an adaptive sparse deconvolution (ASD) method is proposed to overcome these limitations. First, the Gaussian echo model is employed to adaptively estimate the column prototype of the convolution matrix instead of directly using the input signal as the prototype. Then, the convolution matrix is constructed upon the estimated results. Third, the split augmented Lagrangian shrinkage (SALSA) algorithm is introduced to solve the deconvolution problem with high computational efficiency. To verify the effectiveness of the proposed method, guided wave signals obtained from pipeline inspection are investigated numerically and experimentally. Compared to conventional sparse deconvolution methods, e.g. the l_1-norm deconvolution method, the proposed method shows better performance in handling the echo overlap problem in the guided wave signal.

Keywords: non-destructive testing, ultrasonic guided waves, pipeline inspection, adaptive sparse deconvolution

(Some figures may appear in colour only in the online journal)

1. Introduction

Pipelines are widely used in the fields of petroleum, chemicals, aerospace, nuclear power, etc. Many of these pipelines carry valuable or hazardous liquids such as petrochemicals or

nuclear reactor coolant, and any leakage of these substances could result in serious environmental problems and enormous economic losses. Therefore, the non-destructive testing (NDT) of pipelines has become an important discipline for infrastructure management. Using ultrasonic guided waves is an effective method for long-range pipeline inspection; it has received considerable attention [1–4] and has been exploited successfully from a commercial point of view [5]. In guided wave pipeline inspection, the guided waves are emitted by active sensors which propagate along the pipeline structure under inspection. At each discontinuity that the guided wave meets, an echo is reflected and captured by sensors. Therefore, the captured signals contain abundant information as to the interference existing in the path of wave propagation, such as that relating to structural damage. Theoretically, some changes always occur in the observed signals when damage exists. The aim of inspection is to correctly find out about these changes and then associate them with the physical properties of the damage, such as its location and size [6, 7]. However, if the distance between different features is shorter than half the bandwidth of the incident pulse, the reflected echoes may overlap, meaning that the useful information is lost. Moreover, the reflected echoes from small defects can be completely or partly drowned in noise due to their small amplitudes. Besides this, the existence of dispersion, multiple wave modes and broadband noise make defect detection in pipelines an extremely challenging problem. Therefore, effective signal processing methods are required to improve the time resolution of the guided wave signal.

As an effective signal processing method for improving the time resolution of the measured signal, deconvolution has been widely used in ultrasonic NDT fields. Hayward *et al* [8] assessed some non-adaptive deconvolution techniques for improving the time resolution of ultrasonic signals. They concluded that the Wiener pulse-shaping filter was a suitable choice for ultrasonic applications. Honarvar *et al* [9] proposed a new deconvolution method based on Wiener filtering and autoregressive (AR) spectral extrapolation to improve the SNR and time resolution of the ultrasonic NDE signals. This method was also employed by Mirahmadi *et al* [10] to solve the overlapping problem in plate-like structure inspection, utilizing the S_0 Lamb wave mode. Although the Wiener filter deconvolution method has obtained satisfactory results with ultrasonic signals, it still has limitations for guided wave signals, because the performance of the Wiener filter depends on the signal-to-noise ratio (SNR) and the effective bandwidth of the input signal. Meanwhile, phase shifts caused by different structural features are also a key factor for deconvolution performance.

According to the theory of convolution, for guide wave inspection, the occurrence of an echo in the observed signal generates a value in the reflection sequence accordingly. Hence, when echoes exist in the measured signal, spikes occur in the reflection sequence correspondingly, and the other values in the reflection sequence will be zeroes. This implies that the reflection sequence will be sparse—i.e. have the fewest non-zero values—and this is a powerful constraint that needs to be exploited for deconvolution. Based on the sparse properties of the reflection sequence, some sparse algorithms, such as sparse deconvolution methods and sparse decomposition techniques, have been developed to improve the time resolution of the ultrasonic signal. In order to recover a sparse spike time series from an ultrasonic signal, the l_1 norm minimization method was applied by O'Brien *et al* [11]. The result shows that the l_1 norm provides a better solution than the l_2 norm minimization scheme. In [12], sparse deconvolution techniques based on l_1 and l_0 regularizations were employed to solve the resolution enhancement problem of the acoustic signal. Both the MP and the approximate Prony sparse deconvolution methods are presented in [13], and the test results indicate that the methods perform well, even for high noise levels. Other sparse deconvolution methods have also been developed to obtain a sparse solution. For example, matching pursuit (MP) [14], basis pursuit (BP) [15] and l_0 norm regularized minimum entropy deconvolution [16] methods have been employed to analyze ultrasonic signals, respectively.

Unfortunately, the aforementioned sparse deconvolution methods are not robust to guided wave signals, because they do not consider the waveform changes caused by the dispersion properties of the guided wave. The prototype of the echo response is an important factor for obtaining good deconvolution results [17]. The results may differ considerably, even when two slightly different prototypes are used. In theory, the input pulse can be selected as the prototype; however, due to the dispersion properties of guided waves, the incident pulse observed by the received sensors usually changes considerably while it propagates along the structure being tested. In practice, the prototype is usually chosen by the operator directly from the measured signal, because the exact nature of the changes in the incident pulse is poorly known. In this case, reproducible deconvolution results cannot be obtained, because the deconvolution method is very sensitive to variations in the prototype, which are caused by the subjective choices.

In this paper, an adaptive sparse deconvolution (ASD) method is proposed to solve the echo overlap problem in the guided wave signal. The time-varying pulse caused by dispersion is adaptively estimated by the Gaussian echo model, instead of being subjectively chosen by the operator directly from the measured signals. Thus, compared with conventional sparse deconvolution methods, the ASD method is robust to the changes caused by dispersion. Furthermore, to reduce computational cost, the split augmented Lagrangian shrinkage algorithm (SALSA) [18] is utilized to restore the reflection sequence from the measured signals. The ASD method is applied to determine the position of the cracks in the pipeline structure to verify its reliability and efficiency. Simulation and experiment demonstrate that the ASD method is effective for distinguishing the overlapping echoes in the guided wave signal.

The remainder of the paper is organized as follows. In section 2, the convolution model of the guided wave pipeline inspection is introduced. In section 3, the theory of the ASD method is presented. In sections 4 and 5, the proposed method is applied to process the simulation and experimental signal, respectively. The conclusions are summarized in section 6.

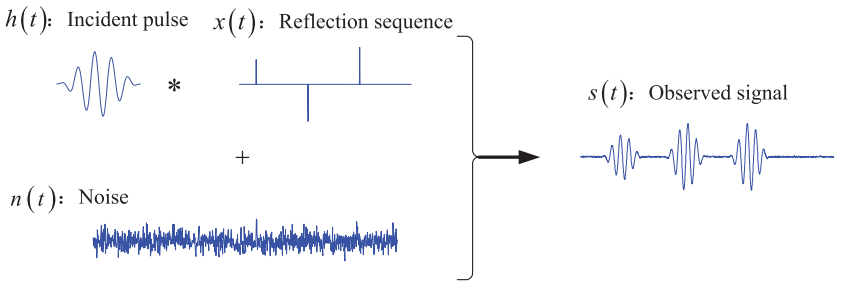

Figure 1. Test signal from guided wave inspection.

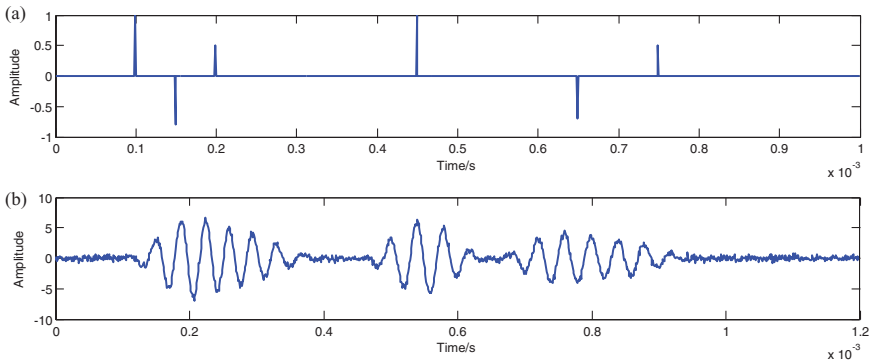

Figure 2. A convolution model of the echo overlapping problem, (a) reflection sequence; (b) test signal.

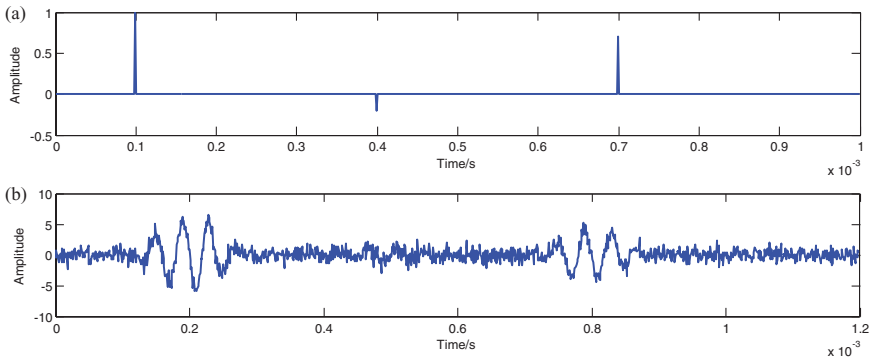

Figure 3. A convolution model of the echo drowning problem, (a) reflection sequence; (b) test signal.

2. Convolution model of guided wave inspection

The measured signal $s(t)$ obtained from the guided wave inspection can be modeled as the convolution of the incident pulse $h(t)$ with the reflection sequence $x(t)$, plus additive noise $n(t)$. The incident pulse $h(t)$ is related to the transducer impulse response and the propagation path. The reflection sequence $x(t)$ is influenced by the characters of the reflector, such as location and size. The convolution model can be represented as

$$s(t) = h(t) * x(t) + n(t) \tag{1}$$

where $x(t)$ and $h(t)$ are the length of N and L, respectively, the measured signal $s(t)$ will be of length $M = N + L - 1$, the noise $n(t)$ is the same length as $s(t)$, and the symbol $*$ denotes the convolution operation. Equation (1) is also illustrated in figure 1, shown as follows.

According to the convolution model, two common problems regarding guided wave inspection will be discussed. The echo overlap problem is shown in figure 2, and each spike in the reflection sequence (as shown in figure 2(a)) represents a defect in the test specimen. Theoretically, there are six spikes in the reflection sequence, thus there should be six reflection echoes in the test signal correspondingly. In fact, only three reflection echoes occur in the test signal—mainly because some of the spikes are very close to each other, leading to the reflection echoes overlapping in a common echo. Another problem is that the reflected echoes from small defects can sometimes be drowned in noise, as shown in figure 3. There are only two clear reflected echoes in the test signal (shown in figure 3(b)), because the amplitude of the second spike is smaller than the other two spikes, which leads to the second reflected echo being completely drowned in noise.

3. The adaptive sparse deconvolution method

The main difference between the ASD method and the previous sparse deconvolution methods is that the prototype of the time-varying pulse caused by dispersion is adaptively estimated by the Gaussian echo model. This guarantees that the ASD method will be more robust to the changes caused by dispersion than conventional sparse deconvolution methods. Meanwhile, the SALSA is employed to obtain better convergence properties.

3.1. Model estimation of incident pulses

An obvious phenomenon caused by dispersion is that the width of the pulse will be extended in the time domain, and the amplitude of the pulse will decrease. The changed pulse can be treated as an energy-attenuated, time-shifted and frequency-dissipated version of the excitation pulse [19, 20]. In this paper, we utilize the Gaussian echo model to analyze the incident pulse. The model can be expressed as

$$f(\theta;t) = \beta e^{-\alpha t^2}\cos(2\pi\omega t + \phi) \tag{2}$$

where $\theta = (\beta, \alpha, \omega, \phi)$ is the parameter vector, β is the amplitude, α expresses the bandwidth factor, ω describes the center frequency, and ϕ is the phase of the pulse. Each parameter has an intuitive meaning for the incident pulse. The amplitude β is related to the properties of the active and received sensors.

The main purpose of this work is to predict the parameter vector $\theta = (\beta, \alpha, \omega, \phi)$ according to the observed incident pulse. The Gauss Newton (GN) algorithm was employed to estimate the parameter of the parameter vector. According to the computing principle of the GN algorithm, the estimation of a parameter vector can be expressed as

$$\theta^{(k+1)} = \theta^{(k)} + (G^T(\theta^{(k)})G(\theta^{(k)}))^{-1}G^T(\theta^{(k)})(h - f(\theta^{(k)})) \tag{3}$$

where $G(\theta)$ is the gradient of the echo model for each parameter in the parameter vector $\theta = (\beta, \alpha, \omega, \phi)$. The whole iteration process of the GN algorithm has the following steps:

1. Choose the initial parameter vector $\theta^{(0)}$, and set the initial number $k = 0$.
2. Compute the gradients $G(\theta^{(k)})$ and the model $s(\theta^{(k)})$.
3. Compute $\theta^{(k+1)} = \theta^{(k)} + (G^T(\theta^{(k)})G(\theta^{(k)}))^{-1}G^T(\theta^{(k)})(h - f(\theta^{(k)}))$.
4. If $\|\theta^{(k+1)} - \theta^{(k)}\| <$ tolerance, then stop.
5. Set $k \rightarrow k + 1$ and go to step 2.

3.2. l_1-norm regularization

According to the principle of mathematical convolution, the operation in equation (1) can be constructed as a matrix multiplication, where one of the inputs is converted into a Toeplitz matrix. Thus, the convolution model of the guided wave inspection (equation (1)) can be formulated as

$$s = Hx + n \tag{4}$$

where H is the convolution matrix. Meanwhile, it is also a Toeplitz matrix of size $M \times N$ with $M > N$. The columns of the Toeplitz matrix are the incident pulse $h(t)$ in the convolution model of the guided wave inspection.

Due to the sparse properties of the reflection sequence x in equation (4), the desired reflection sequence x can be intuitively recovered from the measured signal s by solving

$$\min_x \|x\|_0 \quad \text{subject to } \|s - Hx\|_2^2 \leqslant \delta \tag{5}$$

where $\|x\|_0$ is the l_0-norm of the solution, and is defined as $\|x\|_0 = \sum_m |x_m|_0$, which is used to count the number of nonzero values in x, and the tolerance δ is the noise level. The problem of finding the optimization solution of l_0-norm regularization is NP-hard [21, 22]. Compared with l_2-norm regularization, which controls the energy of the unknown solution, the l_1-norm regularization typically yields a sparse solution, and the reason for this has been proofed in [23, 24]. Thus, Chen in [25] replaces the l_0-norm with the l_1-norm, because minimizing the l_1-norm can help us to find a sparse solution; meanwhile, the l_1-norm is a simple convex problem which can be solved by some classical optimization methods [26, 27]. This transforms the NP-hard problem into a convex optimization problem

$$\min_x \|x\|_1 \quad \text{subject to } \|s - Hx\|_2^2 \leqslant \delta \tag{6}$$

where $\|x\|_1 = \sum_{i=1}^m |x_i|$ is the l_1-norm of the solution. The unconstrained version of equation (6) is given by

$$\arg\min_x \frac{1}{2}\|s - Hx\|_2^2 + \lambda\|x\|_1 \tag{7}$$

where λ is the regularization parameter, which is an important factor for controlling the sparsity of the solution. The method for finding the optimum value of the regularization parameter has been discussed in [12]. The l_1-norm regularization defined in equation (7) is also known as basis pursuit denoising (BPD) [25].

3.3. Split variable augmented Lagrangian shrinkage algorithm (SALSA)

The l_1-norm regularization must be solved by iterative methods due to the lack of an analytic solution; thus, l_1-norm regularization problems can be solved by convex optimization algorithms. Actually, many researchers have made a lot of effort to develop many effective algorithms for solving l_1-norm regularization problems, such as the two-step iterative shrinkage/thresholding algorithm (TwIST) [30], sparse reconstruction by separable approximation (SpaRSA) [31] and SALSA [18, 30]. In this paper the latter is employed to solve the deconvolution problem, because its convergence properties are better than TwIST and SpaRSA in practice [18, 30, 31].

A deconvolution problem like equation (7) is an unconstrained optimization problem, which must be transformed into a constrained optimization problem. Equation (7) can be decomposed into two functions: $f_1(x)$ and $f_2(x)$

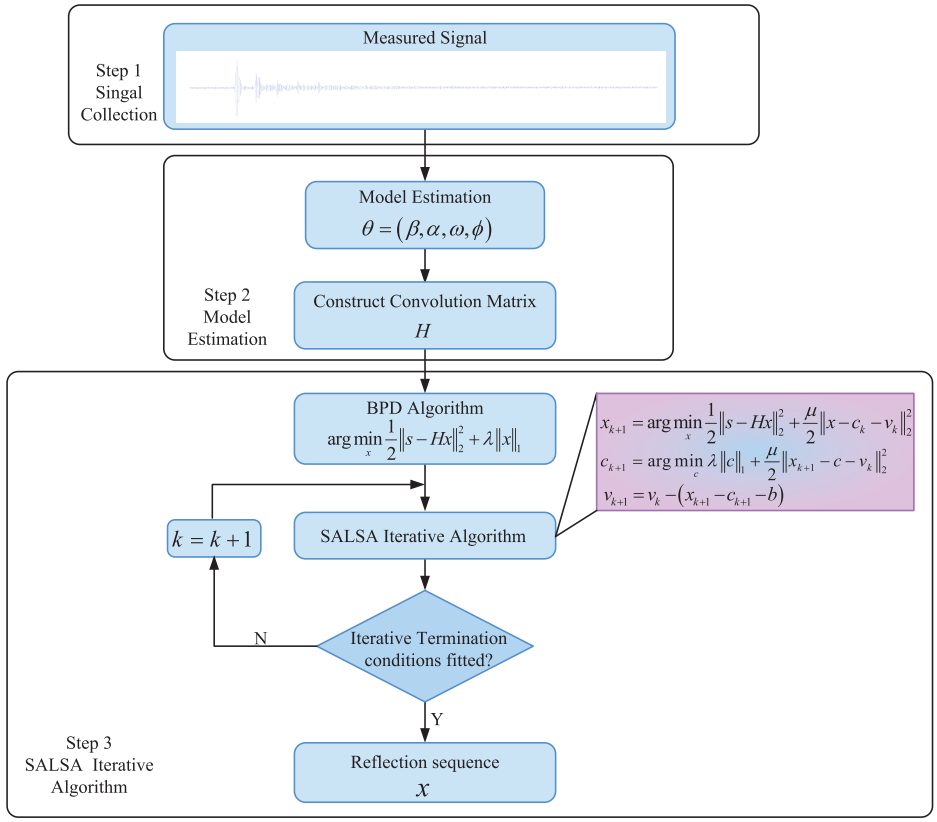

Figure 4. Flow chart of the ASD method.

$$\min_x f_1(x)+f_2(x) \tag{8}$$

where $f_1(x)=\frac{1}{2}\|s-Hx\|_2^2$, $f_2(x)=\lambda\|x\|_1$. Under the constrain $x=c$, equation (8) is equivalent to

$$\min_{x,c} f_1(x)+f_2(c) \quad \text{subject to} \quad x=c \tag{9}$$

which is the so-called variable splitting method. Using the augmented Lagrangian problem to represent this problem as follows

$$\min_z E(z) \quad \text{subject to} \quad Az-b=0 \tag{10}$$

where $E(z)=f_1(x)+f_2(c)$, $z=\begin{bmatrix}x\\c\end{bmatrix}$, $b=0$, $A=[I \quad -I]$. The solution of equation (10) can be written as

$$z_{k+1}=\arg\min_z E(z)+\frac{\mu}{2}\|Az-v_k\|_2^2 \tag{11}$$

$$v_{k+1}=v_k-(Az_{k+1}-b) \tag{12}$$

where k denotes the iteration index and μ is the penalty parameter. Alternating between minimization with respect to x and c, equation (11) can be written as

$$x_{k+1}=\arg\min_x f_1(x)+\frac{\mu}{2}\|x-c_k-v_k\|_2^2 \tag{13}$$

$$c_{k+1}=\arg\min_c f_2(c)+\frac{\mu}{2}\|x_{k+1}-c-v_k\|_2^2. \tag{14}$$

Equations (13) and (14) should be substituted with the explicit form for the two functions f_1 and f_2; then, the SALSA algorithm can be obtained as follows:

$$x_{k+1}=\arg\min_x \frac{1}{2}\|s-Hx\|_2^2+\frac{\mu}{2}\|x-c_k-v_k\|_2^2 \tag{15}$$

$$c_{k+1}=\arg\min_c \lambda\|c\|_1+\frac{\mu}{2}\|x_{k+1}-c-v_k\|_2^2 \tag{16}$$

$$v_{k+1}=v_k-(x_{k+1}-c_{k+1}-b). \tag{17}$$

By running the iterative SALSA until the stopping criterion is satisfied, the solution of equation (7) can be found.

3.4. Adaptive sparse deconvolution

The procedure of the proposed ASD method is illustrated in figure 4. In theory, the columns of the Toeplitz matrix in equation (7) are the input signal. However, the input signal is substantially changed due to the dispersion properties of the guided wave, and the specific changes in the input signals are barely known. Thus, the Gaussian echo model is employed in this paper to estimate the incident pulse in the measured signal. This model is sensitive to the signal characteristics: center frequency, amplitude, bandwidth, and the phase of the incident pulse. Then, the estimation results are used as the columns of the Toeplitz matrix. Compared to the ASD method, the l_1-norm deconvolution method does not have a model estimation procedure (step 2 in figure 4), which is the main

Table 1. The geometric size and material properties of the experimental pipe.

Outer diameter (mm)	Wall thickness (mm)	Young's modulus (GPa)	Poisson's ratio	Mass density (kg m^{-3})
100	1	206	0.29	7850

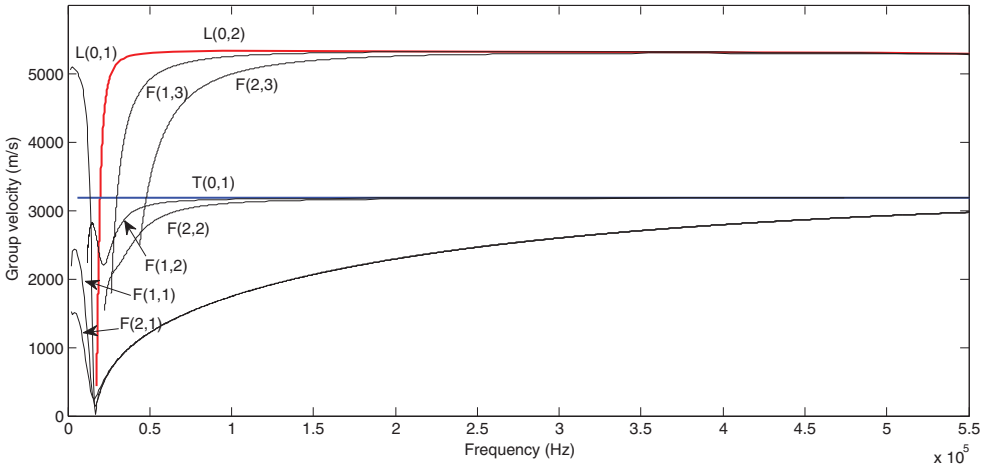

Figure 5. The group velocity dispersion curves for the stainless steel pipe.

difference between the two deconvolution methods. Because of this difference, the time-varying pulse problem caused by dispersion is solved well by the ASD method, whereas it cannot be solved by the conventional l_1-norm deconvolution method.

4. Numerical simulation

In this section, the simulation signals are investigated to verify the effectiveness of the ASD method, and the results are compared with the l_1-norm deconvolution method mentioned in [7]. Moreover, to prove the convergence of the SALSA algorithm, both the TwIST and SpaRSA method are employed.

4.1. Dispersive propagation model

The dispersive propagation model of the guided wave presented in [32, 33] is employed in this paper. A field quantity $f(x,t)$ is used to describe the propagation of the mode of interest in time and space, where x is the propagation distance and t is time. At position $x = 0$, where the transducers are located, $f(x,t) = f(t)$ is the input signal. If the propagation characteristics of the model of interest are known, then $f(x,t)$ can be evaluated at any other point:

$$f(x,t) = \int_{-\infty}^{\infty} F(\omega) \mathrm{e}^{\mathrm{i}(k(\omega)x - \omega t)} \mathrm{d}\omega \tag{18}$$

where $F(\omega)$ is the Fourier transform of the input signal $f(t)$, ω is the angular frequency, the wavenumber $k(\omega)$ is a function of the angular frequency ω, by the simple relationship:

$$k(\omega) = \frac{\omega}{v_{\mathrm{p}}(\omega)}. \tag{19}$$

Substituting equation (19) into equation (18) yields

$$f(x,t) = \int_{-\infty}^{\infty} F(\omega) \mathrm{e}^{\mathrm{i}\left(\frac{\omega}{v_{\mathrm{p}}(\omega)}x - \omega t\right)} \mathrm{d}\omega \tag{20}$$

where v_{p} is the phase velocity of the guided wave mode of interest. Knowing the phase velocity dispersion curve of the pipeline means that $f(x,t)$ can be calculated at any point in time and space.

In practical situations, the received time-trace $y(t)$ usually contains numerous echoes from different features at different positions. In ideal conditions, $y(t)$ can be formulated as the superposition of (18):

$$y(t) = \sum_j \int_{-\infty}^{\infty} A_j F(\omega) \mathrm{e}^{\mathrm{i}\left(\frac{\omega}{v_{\mathrm{p}}(\omega)}x - \omega t\right)} \mathrm{d}\omega + n(t) \tag{21}$$

where A_j is the reflection coefficient of each reflector and $n(t)$ is noise.

4.2. Conditions

In this paper, a stainless steel pipe is selected as the research object, and its geometric size and material properties are shown in table 1. According to the parameters in table 1, the group velocity dispersion curves of the stainless steel pipe are obtained, as shown in figure 5. In total, there are three types of modes in the stainless steel pipe—longitudinal, torsional and flexural—labeled as $L(m,n)$, $T(m,n)$ and $F(m,n)$, respectively. Here the integers m and n denote the circumferential order and group order of a mode. According to the energy distribution in the circumferential direction, these modes can also be divided into two categories: axisymmetric modes ($L(m,n)$ and $T(m,n)$), and non-axisymmetric modes ($F(m,n)$). An axisymmetric mode has the circumferential number $m = 0$. Thus, the longitudinal and torsional modes can be represented as $L(0,n)$ and $T(0,n)$, respectively. In this

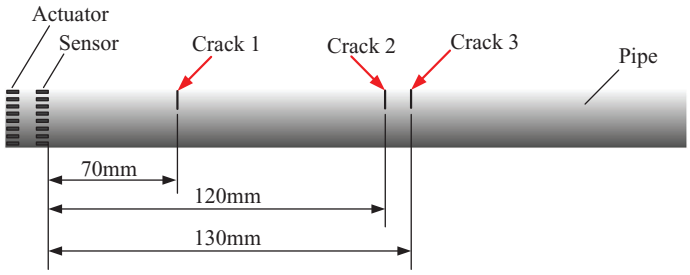

Figure 6. A schematic diagram of the pipe with three cracks.

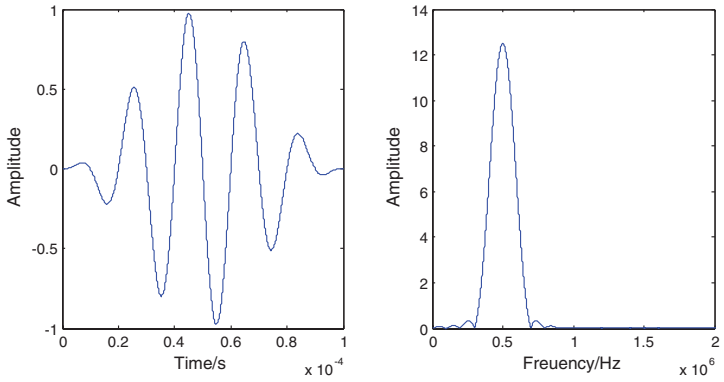

Figure 7. The input signal and its frequency spectrum.

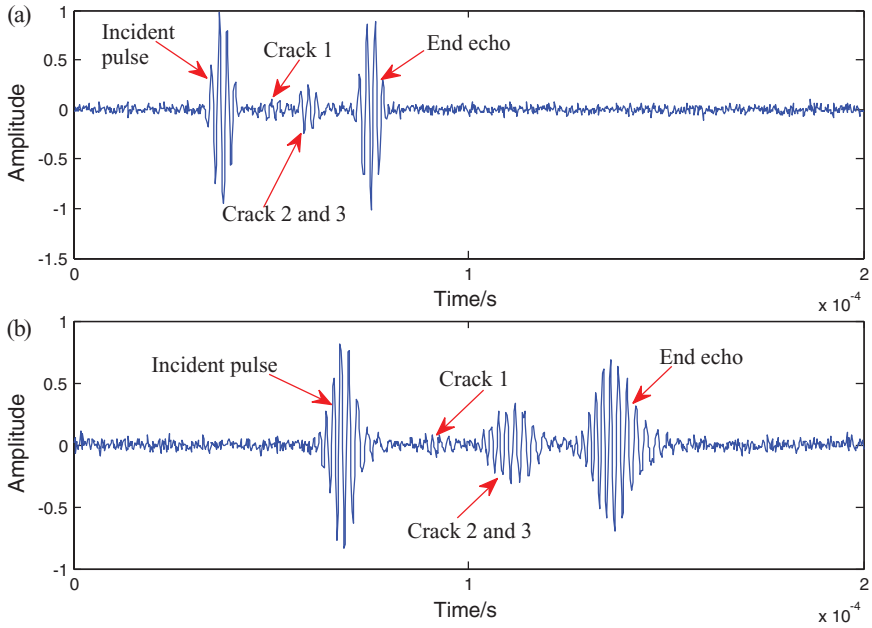

Figure 8. (a) Test result of case 1, (b) test result of case 2.

paper, the $L(0,\mathrm{n})$ modes are selected as our inspection mode, because the direction of particle motion in the $L(0,n)$ modes is perpendicular to the cracks.

Figure 6 shows the geometry of the pipe with three cracks, which are labeled as cracks 1–3. Crack 1 is smaller than the other two cracks. The distance between crack 2 and crack 3 is 10 mm, which is shorter than a wavelength. Two PZT arrays are used as the actuator and sensor, respectively. The input signal is shown in figure 7, where the center frequency is 500 kHz. To compare the stability of the ASD method and the l_1-norm deconvolution method, a simulation study is carried out under dispersion and non-dispersion conditions. In case 1, the $L(0,2)$ mode is used as the input signal, because the dispersion phenomenon does not occur at the center frequency. In case 2, the $L(0,1)$ mode is selected, which shows a clear dispersion phenomenon around the center frequency.

4.3. Results and discussion

The dispersive propagation model shown in equation (20) is employed to illustrate the test results of case 1 and case 2, as shown in figures 8(a) and (b), respectively. Comparing

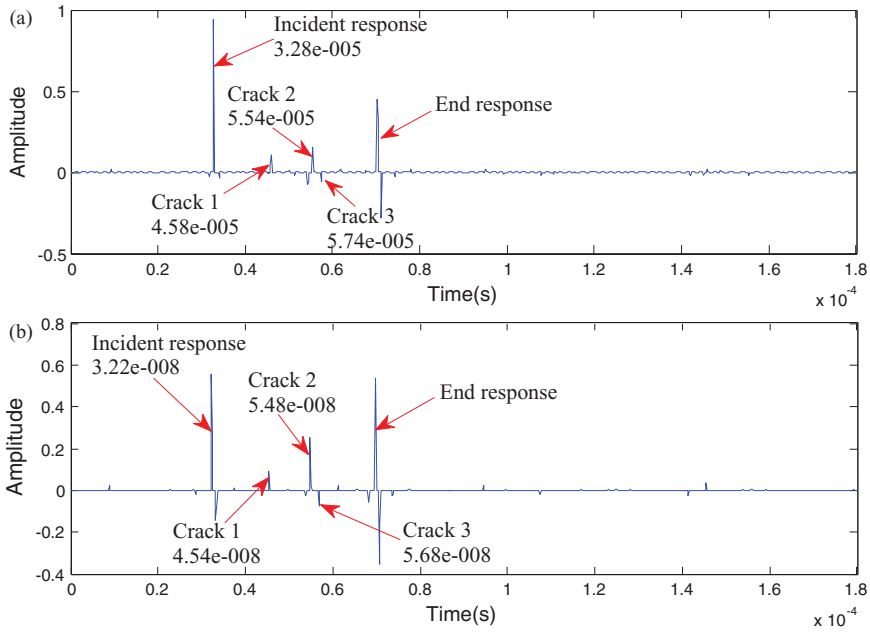

Figure 9. Deconvolution result of case 1, (a) result of the ASD method, (b) result of the l_1-norm deconvolution method.

Table 2. The test results of case 1.

Crack	Distance between the sensor and crack (mm)	Calculation result of the ASD method (mm)	Calculation result of l_1-norm deconvolution method (mm)
Crack 1	70	69.4	70.4
Crack 2	120	120.6	120.6
Crack 2	130	131.2	131.2

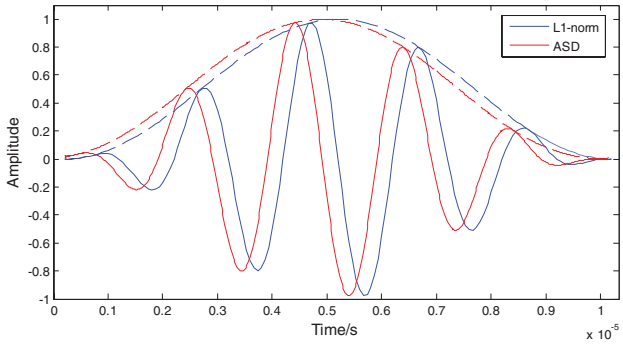

Figure 10. The prototype of the convolution matrix in case 1.

figure 8(b) with (a), in the former it is clear that there is a decrease in the amplitude of the wave-packets and an increase in the width of the pulse in the time domain, caused by the dispersion properties of the $L(0,1)$ mode. Meanwhile, the wave-packets in figure 8(b) obviously lag behind the wave-packets in figure 8(a), because the group velocity of $L(0,1)$ is slower than the $L(0,2)$ mode at the same center frequency.

Theoretically, there should be three echoes in figure 8(a), except the incident pulse and the pipe end echo. However, in fact, there are only two echoes in the received signal, and the echo of crack 1 is unclear as a consequence of its small dimension and low noise level in the test. In addition, the distance between crack 2 and crack 3 is shorter than the half-bandwidth of the incident pulse, leading to the reflected echoes overlapping, resulting in a single common echo. Such

Table 3. Computational cost of three algorithms in case 1.

Algorithm	TwIST	SpaRSA	SALSA
CPU time (s)	10.16	0.546	0.4524

a situation also happens in figure 8(b). It is hard to directly determine the position of the cracks from the original signals without further processing. Thus, the ASD and the l_1-norm deconvolution method are employed to process the test signals of case 1 and case 2, respectively, and the results are shown as follows.

4.3.1. Case 1. From figure 9, it is obvious that the echoes overlap, and the drowning problems are well solved in the two deconvolution results. The echo of crack 1 that drowns in noise is restored, and the overlapping echoes of cracks 2 and 3 are well distinguished. Besides the necessary information about the structural features, there are also some interference components caused by noise in the deconvolution results. According to the time difference between the incident response and the cracks in figure 9(a), and the known group velocity of the $L(0,2)$ mode 5335 m s^{-1}, the distances between the sensor and the cracks are 69.2 mm, 120.6 mm and 131.2 mm, respectively. These results are highly consistent with the crack location shown in figure 5. Comparing figure 9(b) with (a), there is no significant difference in the former.

As can be seen in table 2, the calculation results of the two methods are consistent. This is mainly because the input

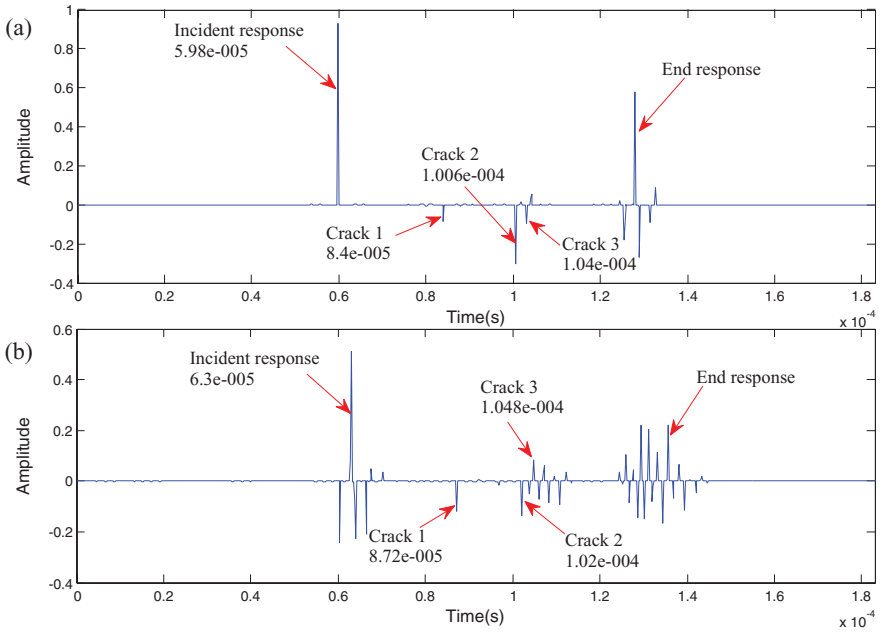

Figure 11. The deconvolution result of case 2, (a) the result of the ASD method, (b) the result of the l_1-norm deconvolution method.

Table 4. Test results of case 2.

Crack	Distance between the sensor and crack (mm)	Calculation result of the ASD method (mm)	Calculation result of the l_1-norm deconvolution method (mm)
Crack 1	70	70.9	70.9
Crack 2	120	119.5	114.4
Crack 3	130	129.5	122.5

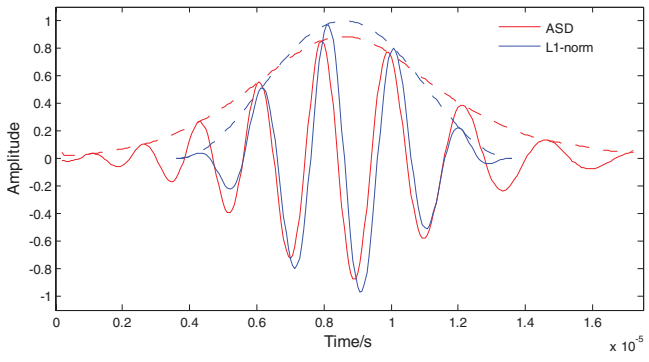

Figure 12. The prototype of the convolution matrix in case 2.

signal is the non-dispersion mode $L(0,2)$, which does not cause large waveform changes in the input signal. The prototype of the columns of the convolution matrix used in the ASD and the l_1-norm deconvolution method are shown in figure 10, and there is no more difference between the two prototypes. Thus, in the absence of dispersion, both the ASD method and the l_1-norm deconvolution method show good performance in improving the time resolution of the guided wave signal. Table 3 shows the CPU times of TwIST, SpaRSA and SALSA in case 1. As excepted, the SALSA is slightly faster than SpaRSA and clearly faster than TwIST when the same stopping criterion (the relative change in the objective function $\frac{1}{2}\|s - Hx\|_2^2 + \lambda\|x\|_1$ falls below 10^{-5}) is satisfied.

Table 5. Computational cost of three algorithms in case 2.

Algorithm	TwIST	SpaRSA	SALSA
CPU time (s)	16.82	0.702	0.5616

4.3.2. Case 2. The deconvolution results of case 2 are shown in figure 11. It is clear that the result of the ASD method is better than the result of the l_1-norm deconvolution method. In figure 11(a), the echoes drown, the overlapping problems are well solved, and the result is sparser than that in figure 11(b). In figure 11(b), although the useful information is recovered from the received signal, there are still a lot of interference components which make the result more complex. The group velocity of the $L(0,1)$ mode at 500 kHz is 2929 m s^{-1}, and the position of the cracks can be determined, as shown in table 4.

From table 4, the crack position calculated by the ASD method is more accurate than that calculated by the l_1-norm deconvolution method, especially for the overlapping echoes. This is mainly because the l_1-norm deconvolution method uses the input signal as the prototype of the columns of the convolution matrix, without considering the waveform changes caused by dispersion. For the ASD method, the prototype of the convolution matrix is adaptively estimated from the received signal, and the difference between the two prototypes is shown in figure 12. Thus, when the dispersion phenomenon exists, the ASD method shows better performance than the l_1-norm deconvolution method. As can be seen from table 5,

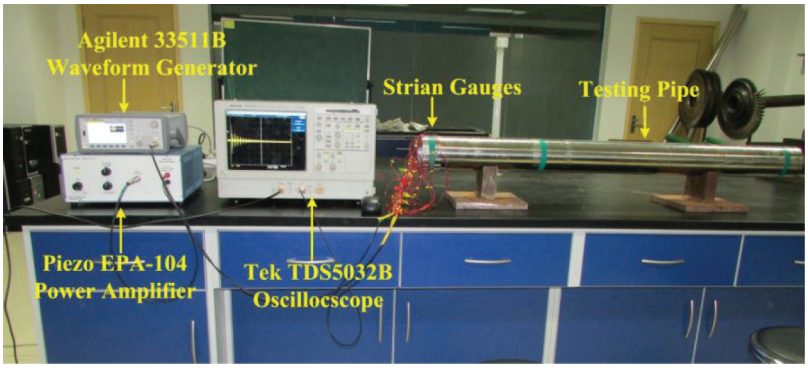

Figure 13. Experimental setup.

for the same convergence condition, the SALSA algorithm is faster than TwIST and SpaRSA.

5. Experimental verification

5.1. Experimental setup

A damage identification system based on the guided waves consists of a signal excitation unit, a data acquisition unit and a certain number of actuators and sensors. The experimental apparatus employed in the test is shown in figure 13. The signal generation subsystem is mainly constructed by an arbitrary waveform generator (Agilent 33511B), a linear power amplifier (PIEZO EPA-104) and an exciter ring, which consists of 16 PZT strain gauges. The role of the signal generation subsystem is to activate the diagnostic guided waves in the pipeline structure. First, the Agilent 33511B arbitrary waveform generator delivers the excitation signal of the desired waveform and central frequency to the PIEZO EPA-104 linear power amplifier; the excitation signal is amplified by the power amplifier in a suitable voltage range. Then the amplified excitation signal is sent to the exciter ring to convert the electrical excitation into a mechanical drive to activate the waves that can travel along the structure. The data acquisition subsystem is composed of a digital oscilloscope (Tek TDS5032B) and a receiver ring whose elements and number of units are the same as the exciter ring. The main purpose of the data acquisition subsystem is to receive guided waves after their propagation in the test structure. The PZT elements of the receiver ring, which serve as sensors, receive the dynamic responses of the test structure. Then the signal from the receiver ring is transferred to the TDS5032B digital oscilloscope for capture.

The stainless steel pipes in this experiment are the same as the pipe mentioned in section 4.2; the geometric size and material properties of the experimental pipes are shown in table 1. In total, there are two groups of test pipe samples with defects labeled as cases 1 and 2, as shown in figure 14. There is only one crack in the test pipe in case 1, and case 2 has three artificial cracks. The pipe samples are all 1200 mm, and the cracks are located at different positions in the test samples. The distance between the receiver rings and the cracks is shown in the figure. In case 2, the radial depths of the cracks are 0.3 mm (crack *A*), 0.6 mm (crack *B*) and 0.9 mm (crack *C*), respectively.

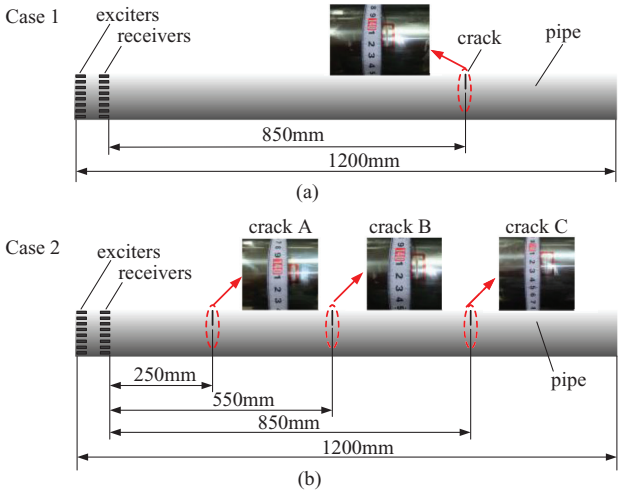

Figure 14. (a) Case 1: the distance between the receiver ring and the crack is 850 mm, (b) case 2: the distance between the receiver ring and the cracks is 250 mm, 550 mm and 850 mm, respectively.

5.2. Model selection

To make the test signal easy to interpret, it is better to excite a single non-dispersive mode in the guided wave inspection. At the same time, it is also essential to utilize the fast mode because it is helpful to separate the signals of interest from the rest of the measured signals in the time domain [34, 35]. The group velocity dispersion curves for the stainless steel pipe (as shown in figure 6) show that the $L(0,2)$ is the fastest mode, and at frequencies of around 70 kHz it is practically non-dispersive. Therefore, this mode is well suited for our application and satisfactory results can be obtained in the frequency range 50–100 kHz. Meanwhile, to guarantee that the desired mode can only be excited in the interested frequency region, the incident pulse can be obtained by employing a sinusoidal signal modulated using a Hanning window [36], as shown in figure 7(a).

5.3. Experimental results

5.3.1. Case 1. The test result of case 1 is shown in figure 15, and the fitting result of the incident pulse in case 1 is shown in figure 16. In the original test signal (figure 15(a)), the crack echo is partly drowned in noise, and thus it is hard to

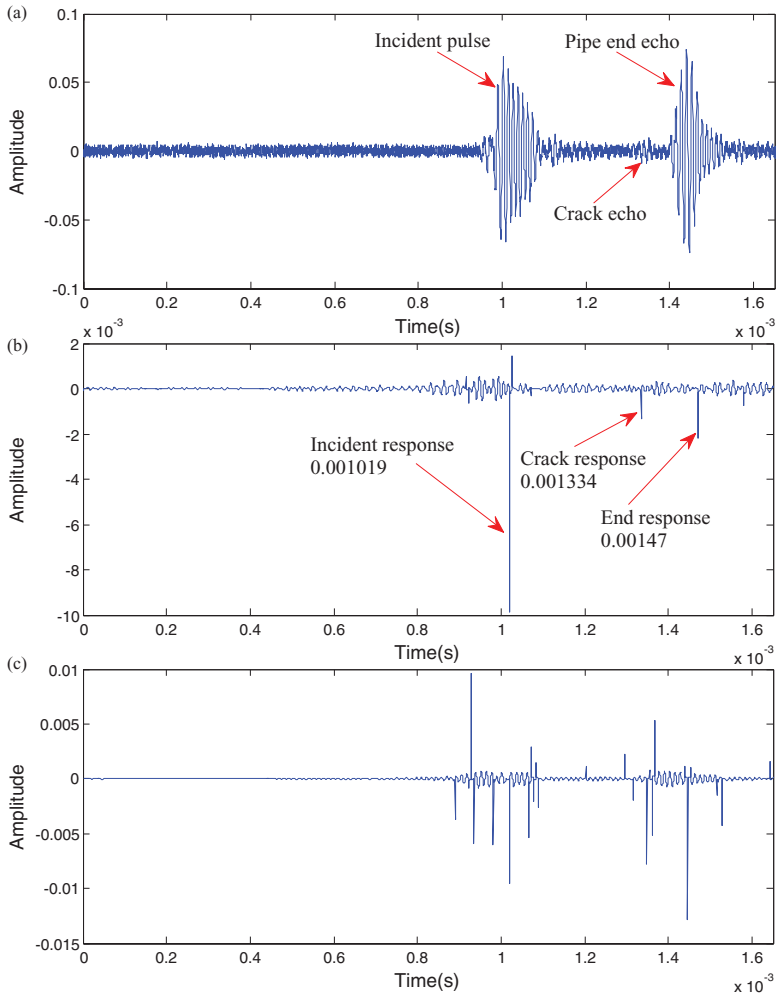

Figure 15. Test result of case 1, (a) the original test signal, (b) the result of the ASD method, (c) the result of the l_1-norm deconvolution method.

determine the position of the crack because of the lack of time resolution. The original test signal is processed by the ASD and the l_1-norm deconvolution method, respectively, and the result is shown in figures 15(b) and (c). Obviously, the result of the ASD method is better than that of the l_1-norm deconvolution method. In figure 15(b), there are only three spikes, namely the incident response, crack response and end response, respectively. The group velocity of the $L(0,2)$ mode is 5335 m s^{-1}, and according to the time difference shown in figure 15(b), the position of the crack and the length of the pipe can be calculated as 840.3 mm and 1203 mm, respectively. The calculation result is highly consistent with the actual situation. Moreover, the result also contains a lot of interference components, which make the deconvolution result more complex, as shown in figure 15(c). Thus, it is difficult to obtain useful information from the deconvolution result of the l_1-norm deconvolution method.

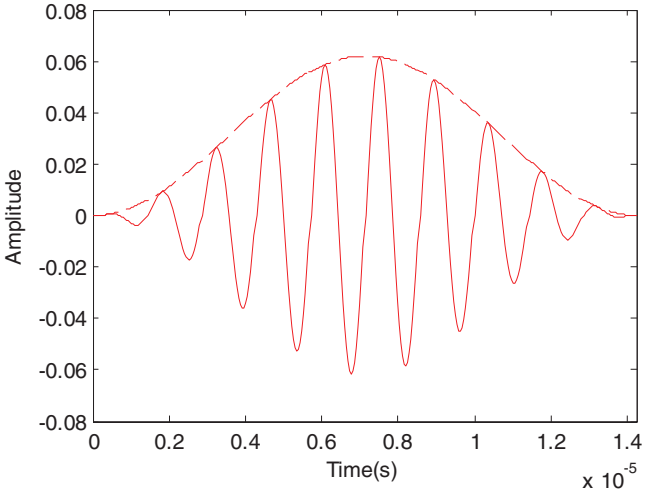

Figure 16. The fitting result of the incident pulse in case 1.

5.3.2. Case 2. In case 2, three artificial cracks are located at different positions in the test pipeline, as shown in figure 17. In theory, there should be three reflected echoes in the original test signal (figure 17(a)) correspondingly. In fact, there are only two crack echoes in the test signal, apart from the incident pulse and pipe end echo. The echo of crack *A* is hard to identify, because it completely overlaps the incident pulse. The echoes of cracks *B* and C are hazy because of noise. In order to distinguish the overlapping echoes and restore those that have been drowned from the noise, the ASD and the

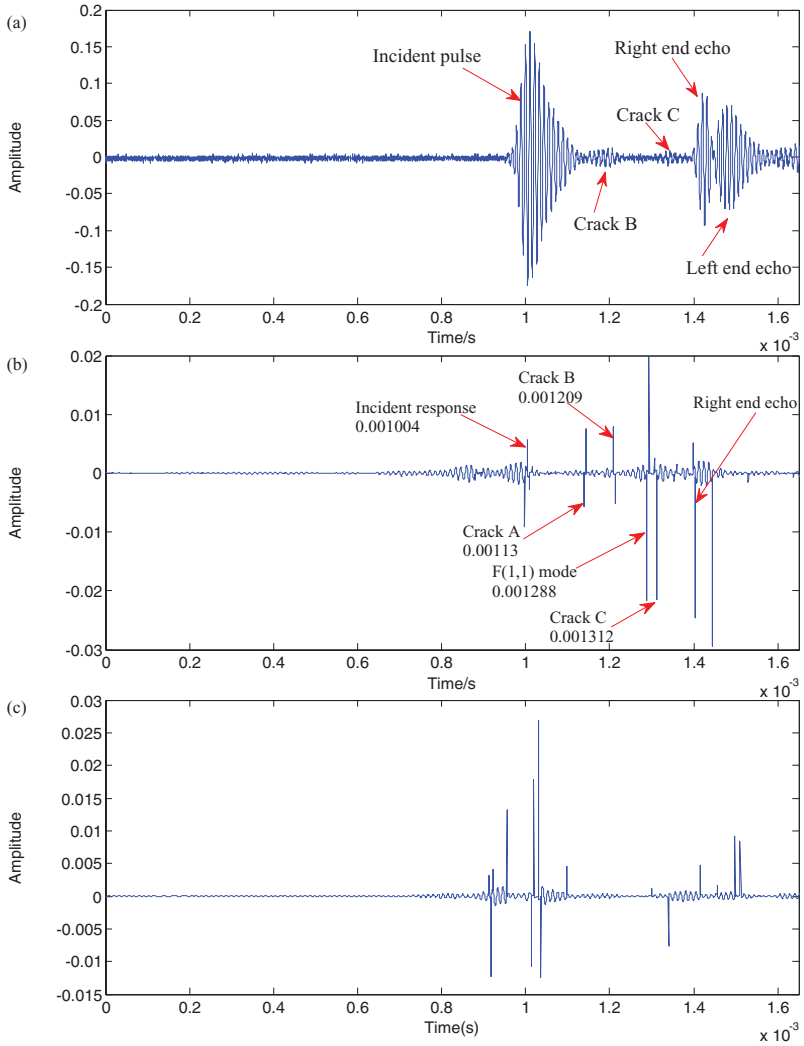

Figure 17. The test result of case 2, (a) the original test signal, (b) the result of the ASD method, (c) the result of the l_1-norm deconvolution method.

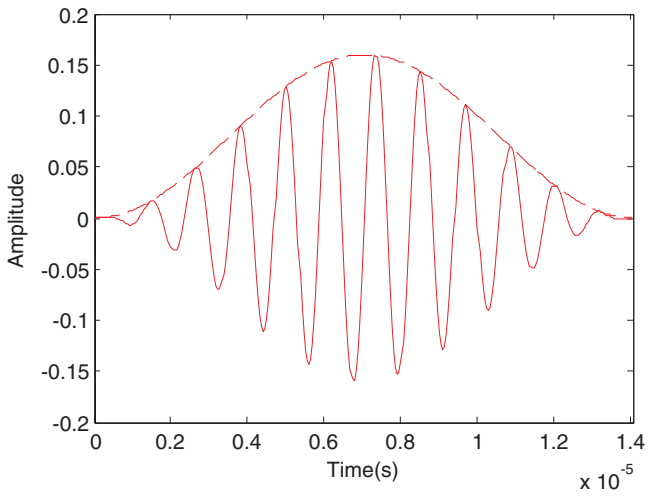

Figure 18. The fitting result of the incident pulse in case 2.

Table 6. Computation cost of the three algorithms in the experiment.

Algorithm	CPU time in case 1 (s)	CPU time in case 2 (s)
TwIST	5.975	13.62
SpaRSA	2.621	2.59
SALSA	1.825	1.716

Table 7. Test results of the experiment.

Case		Distance between the receiver ring and crack (mm)	Measured distance (mm)	Error (%)
1		850	840.3	1.14
2	Crack *A*	250	336.1	34.4
	Crack *B*	550	546.8	0.58
	Crack *C*	850	821.6	3.34

l_1-norm deconvolution method are used to process the original test signal; the results are shown in figures 17(b) and (c), respectively. The fitting result of the incident pulse in case 2 is shown in figure 18.

In figure 17(b), the overlapping echoes are well distinguished and the echoes that have been drowned in noise are also restored. According to the time difference shown in figure 17(b), the position of the cracks can be determined: the positions are 336.1 mm, 546.3 mm and 821.6 mm, respectively. The spike next to crack *C* is the *F*(1,1) mode, which is caused by mode conversion when the *L*(0,2) mode arrives in crack *A*. The time difference between crack *A* and the interference spike is 0.000 158 s, the distance between crack *A* and the sensor is 250 mm, and then the velocity of the wave packet is 1582.3 m s^{-1}. At the excitation frequency, the group velocity of the *F*(1,1) mode is 1574 m s^{-1}, considering the error in the arrival time of the echo in crack *A*; thus, the spike next to crack *C* is the *F*(1,1) mode. As can be seen in figure 17 (c), the deconvolution result of the l_1-norm deconvolution method is grossly distorted. The result contains too much interference component leading to it not being not sparse enough. Meanwhile, the necessary information for crack *A* and crack *B* is missed in figure 17(c).

5.4. Discussion

As can be seen from table 7, except for the fact that the measurement error in crack *A* is relatively large, the measurement results of the other cracks are consistent with the actual situation. The main reason for the large error is probably that the cross-section of crack *A* is the smallest one of the three cracks in the same pipe, which makes the echo in crack *A* weak. As a result, the measurement can easily be influenced by noise. In general, the ASD method is better at solving the echo overlap and the drowning problem of the guided wave signal than the l_1-norm deconvolution method. Meanwhile, table 6 shows that the computing speed of the SALSA algorithm is faster than TwIST and SpaRSA for solving the deconvolution problem.

6. Conclusions

In this paper, an ASD method is proposed to overcome the instability problem that occurs in conventional sparse deconvolution methods for guided wave signals. The robustness of the proposed method is obtained by utilizing the Gaussian echo model to adaptively estimate the prototype of the columns of the convolution matrix instead of directly using the input signal or being subjectively chosen by the operator from the inspection data. To obtain good convergence properties, the proposed method uses the SALSA algorithm to solve the sparse deconvolution problem. Both the simulation and the experiment show that the ASD method is more robust regarding the guided wave signal than the conventional sparse deconvolution method. Meanwhile, the proposed method also shows better performance in the convergence rate. Hence, the ASD method is an effective tool for improving the time resolution of guided wave signals.

Acknowledgments

This work has been supported financially by the National Natural Science Foundation of China (grant nos. 61633001, 51505036, 51421004).

References

[1] Rose J L 2002 A baseline and vision of ultrasonic guided wave inspection potential *J. Press. Vessel Technol.* **124** 273–82
[2] Rose J L *et al* 1996 Ultrasonic guided wave NDE for piping *Mater. Eval.* **54** 1310–3
[3] Alleyne D N *et al* 2001 Rapid, long range inspection of chemical plant pipework using guided waves *Key Eng. Mater.* **43** 180–7
[4] Lowe M J S, Alleyne D N and Cawley P 1998 Defect detection in pipes using guided waves *Ultrasonics* **36** 147–54
[5] Lowe M J S and Cawley P 2006 Long range guided wave inspection usage—current commercial capabilities and research directions Department of Mechanical Engineering Imperial College London https://www3.imperial.ac.uk/pls/portallive/docs/1/55745699.PDF
[6] Yang Z B *et al* 2016 Wave motion analysis and modeling for membrane structures via wavelet finite element method *Appl. Math. Modelling* **40** 2407–20
[7] Yang Z *et al* 2014 Wave motion analysis in arch structures via wavelet finite element method *J. Sound Vibr.* **333** 446–69
[8] Hayward G and Leis J E 1989 Comparison of some non-adaptive deconvolution techniques for resolution enhancement of ultrasonic data *Ultrasonics* **27** 155–64
[9] Honarvar F *et al* 2004 Improving the time-resolution and signal-to-noise ratio of ultrasonic NDE signal *Ultrasonics* **41** 755–63
[10] Mirahmadi S J and Honarvar F 2011 Application of signal processing technique to ultrasonic testing of plates by S0 Lamb wave mode *NDT E Int.* **44** 131–7
[11] O'Brien M S, Sinclair A N and Kremer S M 1994 Recovery of a sparse spike time series by L1-norm deconvolution *IEEE Trans. Signal Process.* **42** 3353–65
[12] Soussen C *et al* 2012 Ultrasonic non-destructive testing based on sparse deconvolution *J. Phys: Conf. Ser.* **353** 012018
[13] Boßmann F *et al* 2012 Sparse deconvolution methods for ultrasonic NDT *J. Nondestruct. Eval.* **31** 225–44
[14] Wei L, Huang Z-y and Que P-w 2009 Sparse deconvolution method for improving the time-resolution of ultrasonic NDE signals *NDT E Int.* **42** 430–4
[15] Zhang G, Zhang S and Wang Y 2000 Application of adaptive time-frequency decomposition in ultrasonic NDE of highly-scattering materials *Ultrasonics* **38** 961–4
[16] Li X *et al* 2012 ℓ_0-norm regularized minimum entropy deconvolution for ultrasonic NDT & E *NDT E Int.* **47** 80–7
[17] Olofsson T 2004 Semi-sparse deconvolution robust to uncertainties in the impulse responses *Ultrasonics* **42** 969–75
[18] Afonso M V, Bioucas-Dias J M and Figueiredo M A T 2010 Fast image recovery using variable splitting and constrained optimization *IEEE Trans. Image Process.* **19** 2345–56
[19] Demirli R and Saniie J 2001 Model-based estimation of ultrasonic echoes. Part I: analysis and algorithms *IEEE Trans. Ultrason. Ferroelectr. Freq. Control* **48** 787–802
[20] Demirli R and Saniie J 2001 Model-based estimation of ultrasonic echoes. Part II: Nondestructive evaluation applications *IEEE Trans. Ultrason. Ferroelectr. Freq. Control* **48** 803–11
[21] Idier J (ed) 2013 *Bayesian Approach to Inverse Problems* (New York: Wiley) pp 117–37

[22] Qiao B J *et al* 2017 Sparse deconvolution for the large-scale ill-posed inverse problem of impact force reconstruction *Mech. Syst. Signal Process.* **83** 93–115
[23] Kutyniok G 2013 Theory and applications of compressed sensing *GAMM-Mitt.* **36** 79–101
[24] Jacques L and Vandergheynst P 2010 *Compressed Sensing: When Sparsity Meets Sampling* (Weinheim: Wiley-Blackwell)
[25] Chen S S, Donoho D L and Saunders M A 1998 Atomic decomposition by basis pursuit *SIAM J. Sci. Comput.* **20** 33–61
[26] Qiao B J *et al* 2016 Impact-force sparse reconstruction from highly incomplete and inaccurate measurements *J. Sound Vibr.* **376** 72–94
[27] Qiao B J *et al* 2016 Sparse regularization for force identification using dictionaries *J. Sound Vibr.* **368** 71–86
[28] Bioucas-Dias J M and Figueiredo M A T 2007 A new twist: two-step iterative shrinkage/thresholding algorithms for image restoration *IEEE Trans. Image Process.* **16** 2992–3004
[29] Wright S J, Nowak R D and Figueiredo M A T 2008 Sparse reconstruction by separable approximation *IEEE Trans. Signal Process.* **57** 3373–6
[30] Afonso M V, Bioucas-Dias J M and Figueiredo M A T 2011 An augmented Lagrangian approach to the constrained optimization formulation of imaging inverse problems *IEEE Trans. Image Process.* **20** 681–95
[31] He W P *et al* 2016 Sparsity-based algorithm for detecting faults in rotating machines *Mech. Syst. Signal Process.* **54** 457–80
[32] Wilcox P D 2003 A rapid signal processing technique to remove the effect of dispersion from guided wave signals *IEEE Trans. Ultrason. Ferroelectr. Freq. Control* **50** 419–27
[33] Zeng L and Lin J 2014 Chirp-based dispersion pre-compensation for high resolution Lamb wave inspection *NDT E Int.* **61** 35–44
[34] Alleyne D N and Cawley P 1996 The excitation of Lamb waves in pipe using dry-coupled piezoelectric transducers *J. Nondestruct. Eval.* **15** 11–20
[35] Alleyne D N and Cawley P 1992 Optimization of Lamb wave inspection techniques *NDT E Int.* **25** 11–22
[36] Alleyne D and Cawley P 1994 The practical excitation and measurement of Lamb waves using piezoelectric transducers *Rev. Prog. Quant. Nondestruct. Eval.* **13** 181